FISEVIER

Contents lists available at ScienceDirect

### Journal of Alloys and Compounds

journal homepage: www.elsevier.com/locate/jalcom



# Effect of Mo addition on structures and properties of FeCoNiCrMn high entropy alloy film by direct current magnetron sputtering



Yiman Zhao<sup>a</sup>, Xiaomin Zhang<sup>b</sup>, Hui Quan<sup>a</sup>, Yujie Chen<sup>a,c</sup>, Shu Wang<sup>a</sup>, Sam Zhang<sup>a,\*</sup>

- <sup>a</sup> Center for Advanced Thin Films and Devices, School of Materials and Energy, Southwest University, Chongaing 400715, China
- <sup>b</sup> School of Resources Engineering, Xi'an University of Architecture and Technology, Xi'an, Shaanxi 710049, China
- <sup>c</sup> School of Mechanical Engineering, The University of Adelaide, Adelaide, SA 5005, Australia

### ARTICLE INFO

Article history: Received 16 September 2021 Received in revised form 31 October 2021 Accepted 8 November 2021 Available online 15 November 2021

Keywords: FeCoNiCrMnMo<sub>x</sub> HEA thin film Body-centered-cubic Face-centered-cubic Hardness Tribological

### ABSTRACT

FeCoNiCrMnMo $_{\rm x}$  high-entropy alloy (HEA) films were prepared by direct current (DC) magnetron cosputtering. The influence of the Mo content on the microstructures and mechanical properties of the HEA films were systematically studied by X-ray diffraction (XRD), field emission scanning electron microscope (FESEM), Vickers hardness test and tribological test. The addition of Mo results in the formation of a denser film with refined grain size, and promotes the transformation from a face-centered cubic (FCC) phase to a mixture of FCC and body-centered cubic (BCC) phases. The hardness of the films increases from 8.5 GPa (x = 0) to 12 GPa (x = 1) and the friction coefficient decreases from 0.5 (x = 0) to 0.3 (x = 1), which greatly enhance the damage tolerance of the film. The improved mechanical and tribological properties of the HEA films are attributed to the formation of the hard BCC phase and grain refinement at high contents of Mo. The FeCoNiCrMnMo $_{\rm x}$  HEA films are suitable candidates for structural application as protective coatings.

© 2021 Elsevier B.V. All rights reserved.

### 1. Introduction

High-entropy alloys (HEAs) is a category class of alloys, consisted of at least five principal elements in equiatomic or near equiatomic concentrations [1,2]. HEAs possess excellent properties due to its four core effects: high entropy effect, sluggish diffusion, lattice distortion and cocktail effects [3,4]. In contrast to the most traditional binary and ternary alloys, HEAs have a disposition to form simple single-phase solid solution phase with face-centered cubic (FCC) structure, body-centered cubic (BCC) structure, densely arranged hexagonal closed-packed (HCP) structure or amorphous structure, rather than intermetallic compounds [5]. HEA films is a new type of films developed on the basis of HEA concept. HEA films exhibit many excellent properties, including high strength and hardness [6], excellent wear resistance [7], corrosion resistance [8], irradiation resistance [9,10], high toughness [11], and thermal stability [12], which are incomparable by traditional films.

As one of the most-studied HEAs, the FCC structured "Cantor alloy" or FeCoNiCrMn HEA exhibits excellent mechanical properties, such as high fracture toughness and strong creep resistance [13]. Like most FCC structured alloys, the Cantor alloy shows high

\* Corresponding author. E-mail address: samzhang@swu.edu.cn (S. Zhang). ductility but low yield strength, usually below 400 MPa at 293 K [13,14]. Moreover, as compared with other HEA films, the Cantor alloy film shows relatively low hardness. The hardness of the Cantor alloy coatings prepared by plasma spraying and magnetron sputtering were found to be ~270 HV and ~6 GPa, respectively [15,16]. In addition, the friction coefficient of the Cantor alloy film is very high at ~0.7. Therefore, it is imperative to enhance the hardness and friction properties of the Cantor alloy films for practical applications.

Alloying has been used to tune various properties of materials for a long time. Previous studies have shown that alloying additions, such as N, Al, Mo, W, Si and C can be used to improve the mechanical properties of HEAs [17–19]. Xin et al. have reported that the addition of Si in the FCC structured Al<sub>0.2</sub>Co<sub>1.5</sub>CrFeNi<sub>1.5</sub>Ti<sub>0.5</sub> HEA improved its hardness due to the formation of hard silicide and the interstitial solid solution strengthening of Si, but reduced its compressive strength and fracture toughness [20]. Ya et al. reported that owing to the addition of Al in the CoCrFeMnNiAl<sub>x</sub> films, the formation of nanotwins and BCC phases contribute to the strengthening effect of these HEA films [18].

It has been reported that the addition of Mo in CoCrFeNi or Al<sub>2</sub>CrFeNi with relatively large atomic radius (0.14 nm) not only improved the film strength and hardness through substitutional solid solution strengthening, but also reduced the wear rate of the film because of the formation of an oxide film on surface of the film that provides lubrication effect [21,22]. Furthermore, the yield

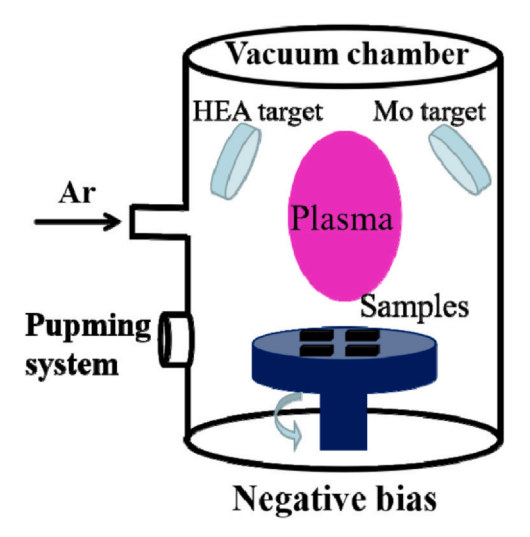


Fig. 1. Schematic diagram of the direct current magnetron sputtering deposition system.

strength of the bulk Cantor alloy significantly increased with the addition of Mo, attributed to the phase transformation from an FCC phase to  $\sigma$  phase promoted by the addition of Mo [23]. Therefore, we suspected that the mechanical properties of the Cantor alloy films could also be enhanced by the addition of Mo, making them suitable candidates for structural applications in harsh environment. Till now, there is only one very recent study [24] focusing on the yield strength and fracture strain of a Mo-doped Cantor alloy film.

In this study, five compositions of Mo are doped into FeCoNiCrMn to form FeCoNiCrMnMo $_{\rm x}$  (x = 0, 0.25, 0.6, 0.8, 1) HEA films using magnetron co-sputtering of a Cantor alloy target and a Mo target at different powers (Fig. 1). As FeCoNiCrMn high entropy alloy is often referred to as Cantor alloy, we will adopt this and refer Cantor alloy in place of FeCoNiCrMn, and will refer FeCoNiCrMnMo $_{\rm x}$  as Mo-doped Cantor alloy to stay conceptually clearer. X-ray diffraction (XRD), field-emission scanning electron microscope (FESEM) and nanoindentation are employed and the microstructures, compositions, mechanical properties, and wear properties were systematically investigated. It was found that with increase of Mo, the hardness increased and the friction coefficient decreased. The relationship between the microstructure, mechanical properties, and wear resistance is discussed in detail.

### 2. Materials and methods

FeCoNiCrMnMo $_{\rm x}$  HEA films were deposited by co-sputtering a Cantor alloy target (FeCoNiCrMn) and a Mo target (101.6 mm in diameter), both of purity higher than 99.9 wt%. More details on the co-sputter deposition system are provided elsewhere [25]. Silicon wafers and 304 stainless steels were used as substrates. Prior to deposition, the substrates were cleaned using acetone, ethanol and deionized water in sequence, with each step being 15 min. The base pressure of the deposition chamber was pumped to below  $3\times 10^{-6}$  Torr. In order to remove possible contaminations on the target

surface and to balance the surface composition of the targets, the Cantor alloy target and the Mo target were pre-sputtered using Ar<sup>+</sup>-ion bombardment for 15 min. The deposition of the CoCrFeMnNiMo<sub>x</sub> thin films was performed at a chamber pressure of  $3.9\times 10^{-3}$  Torr. The power of the HEA target was fixed at 400 W, while the power of the Mo target varied from 0 to 90 W to adjust the Mo content in the deposition films. The substrate was rotated at 15 Round/min to ensure homogeneity in elements distribution. The substrate bias power is 50 W. The deposition time was controlled to ensure a uniform thickness of ~1  $\mu m$  for all films.

The crystalline structures and compositions of the films were examined by X-ray diffraction (Rigaku TTRAX 3) with Cu  $K\alpha$ ( $\lambda = 0.15406 \text{ nm}$ ) radiation, scanning angle, 20, ranged from 20° to 100° and the electron probe X-ray microanalyzer (EPMA, JEOL JXA-8200). The surface morphology and film thickness were analyzed using a thermal field emission scanning electron microscope (ISM-7800 F(JEOL)). The hardness was surveyed by Hysitron TI 950 Triboindenter (Bruker, Minneapolis, MN, USA) using a Berkovich indenter with a tip radius of 100 nm. In order to eliminate the influence of the substrate on the measurements, the indentation depth was less than 1/10 of the thickness of all the films. The tests were repeated at least five times to reduce errors. The friction and wear properties of the resultant films were analyzed by using a ball-ondisc friction and wear tester (MF TR-4000, China), with an additional force of 1 N and a friction time of about 30 min. The wear test was repeated three times.

### 3. Results

## 3.1. Compositions and Crystalline Structure of the FeCoNiCrMn $Mo_x$ HEA films

The Cantor alloy target has an elemental composition (at%) of  $20.88 \pm 1.43\%$  of Fe,  $20.04 \pm 1.07\%$  of Co,  $18.39 \pm 0.78\%$  of Ni,  $20.74 \pm 0.90\%$  of Cr, and  $19.95 \pm 0.65\%$  of Mn. The contents of Fe, Co, Ni, Cr and Mn were approximately equivalent to the nominal equiatomic percentage of 20 at%. The chemical compositions of the resultant HEA films are presented in Table 1. We assumed that the contents of six elements (Fe, Co, Ni, Cr, Mn and Mo) were equivalent to the nominal equiatomic percentage of 16.67 at%. Thus, according to the different Mo content in the film, it was named as Mo<sub>0</sub>, Mo<sub>0.25</sub>, Mo<sub>0.6</sub>, Mo<sub>0.8</sub> and Mo<sub>1</sub>. The element content in the Mo<sub>0</sub> film was different from that of the Cantor alloy target owing to different sputter yields of each element [26]. The Mo content of the films increased as sputtering power of the Mo target increased from 0 to 90 W. Fig. 2 shows the surface distribution of each element in the  $Mo_{0.6}$  film. It can be seen that all elements, i.e., Fe, Co, Ni, Cr, Mn and Mo, are uniformly distributed across the sample surface.

The surface morphology of the Mo-doped Cantor alloy films is shown in Fig. 3. As is shown, there are some pores on the films. When the Mo content increased, the film became denser, evidenced by the reduced diameter of the pores on the film surfaces. The cross sectional FESEM images of the Mo-doped Cantor alloy films are presented in Fig. 4, showing a columnar structure for all films, similar in other literatures [27]. There are no defects and cracks

 Table 1

 Elemental composition of resultant Mo-doped Cantor alloy films.

Mo/Power (W)	Fe (at%)	Co (at%)	Ni (at%)	Cr (at%)	Mn (at%)	Mo (at%)	х
0	22.79	21.76	19.67	22.84	12.94	0	0
20	21.07	22.80	18.92	20.96	11.93	4.32	0.25
50	17.91	19.60	18.90	20.31	11.45	10.84	0.6
70	20.30	19.33	16.15	19.50	10.30	14.43	0.8
90	17.20	18.81	16.75	19.39	11.19	16.67	1

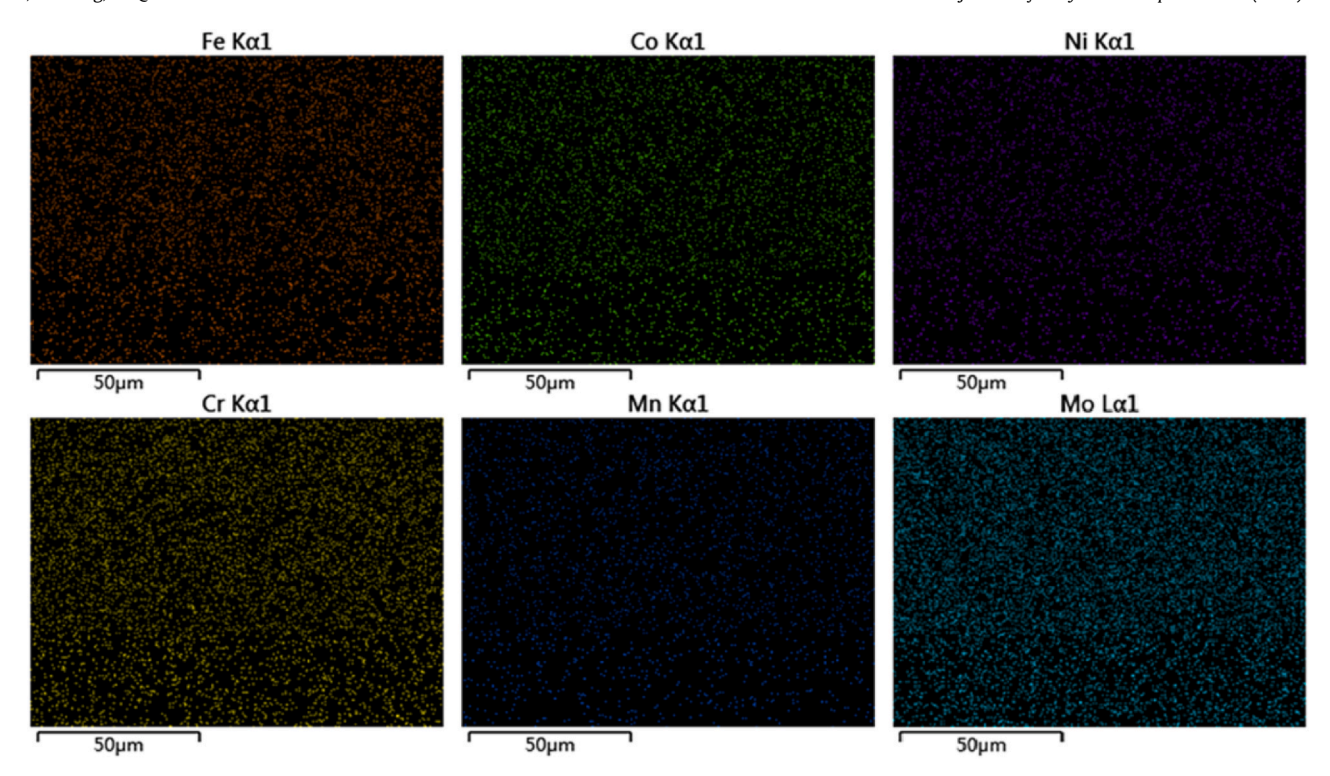


Fig. 2. EDS mapping of the resultant Mo<sub>0.6</sub> film surface. All the elements are uniformly distributed across the sample surface.

observed at the interface, indicating that all the films are well adhered on the substrates.

The XRD results of the HEA films (Fig. 5) show that films present a simple FCC solid solution structure. The diffraction peaks at 43.7°, 51.5°, 74.9° and 90.1° correspond to the (111), (200), (220) and (311) of the FCC phase. This result agreed with previous reports [24], indicating that the FCC solid solution phase with good crystallinity. Additional diffraction peaks observed at 45.9° in the XRD pattern of the film prepared at Mo target of 20 W indicate the formation of the BCC phase caused by the incorporation of Mo. The (200), (220) and (311) diffraction peaks of the FCC phase gradually weakened with increasing the Mo content. At the same time, the diffraction peaks of (110) and (211) of the BCC phase appeared and gradually

strengthened. Thus, the FeCoNiCrMnMo $_{\rm x}$  HEA films exhibit the duplex FCC+BCC phase structure. This result is agreed with reference [14], which showed that the phase structure of the FeCoNiCrMn- Al $_{\rm x}$  film changes from FCC to coexistence of FCC and BCC after doping of Al. Moreover, the full width at half maximum (FWHM) of each peak gradually increased with the increasing of Mo, indicating that the grain size decreased as the Mo content increased [24]. The grain sizes corresponding to each peak of the FCC phase and the BCC phase were calculated by using the Scherrer formula [28]. The crystalline size of resultant Mo-doped Cantor alloy films is listed in Table 2. Obviously, the average grain size decreases with increasing the Mo content, and the smallest grain size was observed in the Mo $_{\rm 1}$  HEA film.

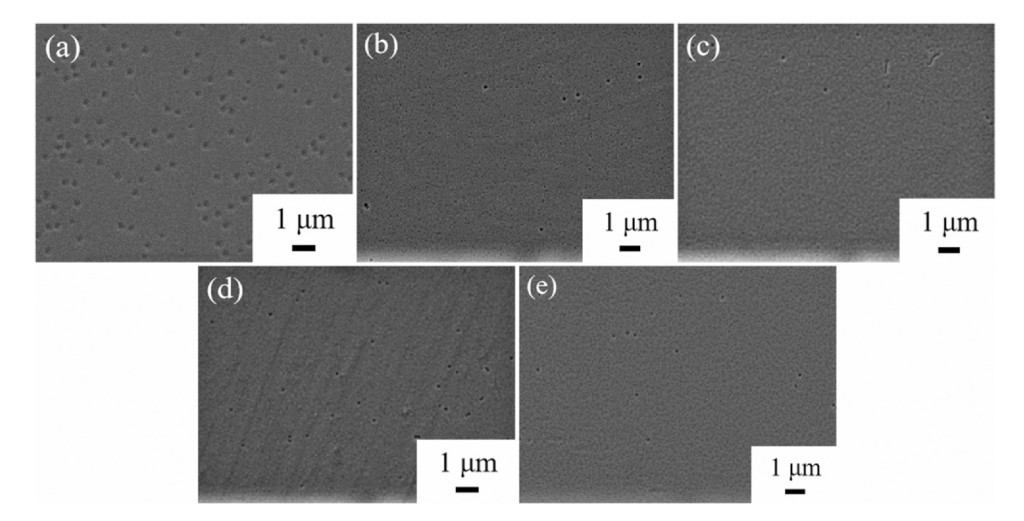


Fig. 3. FESEM images of the surface of FeCoNiCrMnMo $_x$  (x = 0, 0.25, 0.6, 0.8, 1) HEA film. (a)x = 0; (b)x = 0.25; (b)x = 0.25; (c)x = 0.8; (e)x = 0.8; (f)x = 0.8; (f)

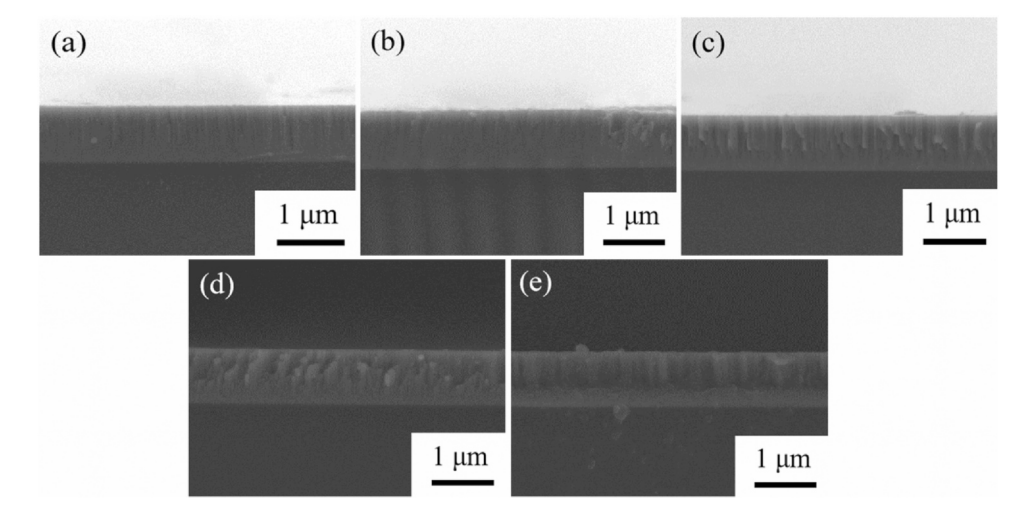
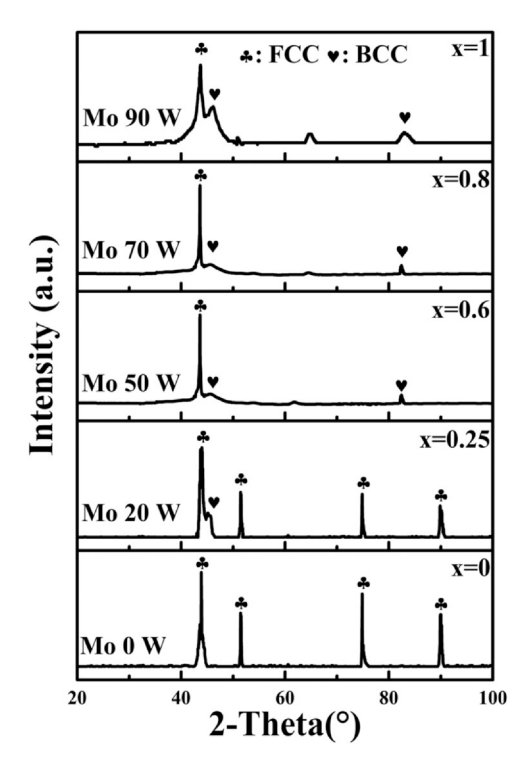


Fig. 4. Cross sectional FESEM images of FeCoNiCrMnMo<sub>x</sub> (x = 0, 0.25, 0.6, 0.8, 1) HEA films. (a)x = 0; (b)x = 0.25; (b)x = 0.6; (d)x = 0.8; (e)x = 1. No defects or cracks were observed at the interface, indicating that all the films are well adhered to the substrates.



**Fig. 5.** XRD patterns of FeCoNiCrMnMo $_{\rm x}$  (x = 0, 0.25, 0.6, 0.8, 1) HEA films. With the addition of Mo, the phase structure of the films changed from a single FCC to the coexistence of FCC and BCC, and the grain sizes synchronously decreases.

**Table 2**The crystalline size of resultant Mo-doped Cantor alloy films.

	Crystal	line size	Average crystalline size (nm)				
	FCC				ВСС		
	(111)	(200)	(220)	(311)	(110)	(211)	
Mo <sub>0</sub>	10.06	38.20	42.90	26.52	-	-	28.90
$Mo_{0.25}$	13.42	30.25	43.63	20.54	6.30	-	22.93
$Mo_{0.6}$	37.63	-	-	-	1.38	23.73	20.95
$Mo_{0.8}$	37.44	-	-	-	1.38	23.70	20.84
$Mo_1$	4.94	-	-	-	6.04	7.27	6.08

The lattice constant of FCC phase structure, atomic size difference  $(\delta)$  and valence electron concentration (VEC) (defined by Eqs. (1) and (2) [29–31]) as a function of the Mo are shown in Fig. 6 showing the lattice constant increased with the increase of Mo content, as the atomic radius of Mo is larger than that of other elements.

$$\delta = 100 \cdot \sqrt{\sum_{i=1}^{n} c_i (1 - r_i/\bar{r})^2}$$
 (1)

$$VEC = \sum_{i=1}^{n} c_i (VEC)_i$$
 (2)

Where n is the number of the constituent elements in the films,  $c_i$  is the atomic percentage of the ith element,  $r_i$  is the atomic radius of the ith element,  $\bar{r} = \sum_{i=1}^n c_i r_i$  is the average value of the atomic radius and (VEC) $_i$  is the VEC of the ith element. The influences of Mo content on the  $\delta$  and VEC is shown in the Fig. 6(b). For Cantor alloy film,  $\delta$  and VEC are ~1.13% and 8.02, respectively. With the addition of Mo element, the  $\delta$  value of the films gradually increased from 1.13% to 4.20% (x = 1), and the value of VEC gradually decreased from 8.02 to 7.69 (x = 1).

The hardness of the films as a function of Mo content are shown in Fig. 7. For the Cantor alloy film, the hardness is around 8.5 GPa, which is higher than the bulk HEA ( $\sim$ 160 HV) [32], and also higher than the Cantor alloy film doped with the other element [18,28]. As the Mo content increased, the hardness of the films gradually increased to  $\sim$ 12 GPa (x = 1).

The friction coefficient (COF) curves for the Mo-doped Cantor alloy films with various Mo content sliding against  $\rm Si_3N_4$  ball are displayed in Fig. 8. It can be seen that the friction coefficient curves of all films increased sharply in the initial stage, which corresponds to the run-in period, and then reached a relatively steady state. The average COF of the film without Mo is around 0.5. The COF of the film gradually decreases with increasing the Mo content, and reaches the minimum value of 0.3. Fig. 9 shows the friction trajectory surface and elemental mapping images of the Mo-doped Cantor alloy films after sliding in the atmosphere. The wear track widths of the films with Mo content of 0, 0.25, 0.6, 0.8 and 1 were 267.92, 237.5, 225.0, 221.67 and 204.17  $\mu$ m, respectively. It can be seen that the films with low Mo contents have more debris and the deeper friction marks on the wear tracks after friction. There are less debris and shallower friction marks on the wear tracks of the film with high Mo content.

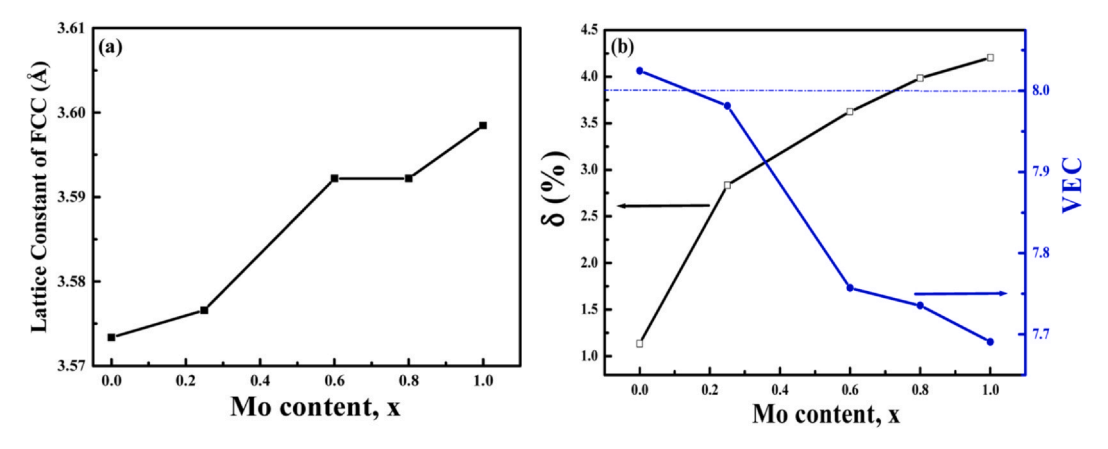
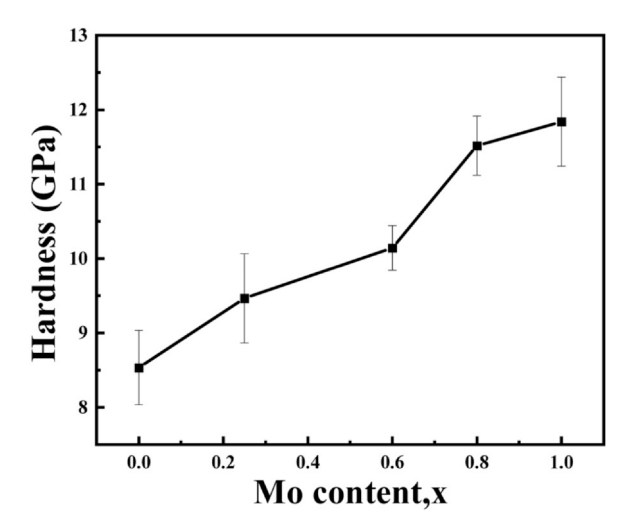
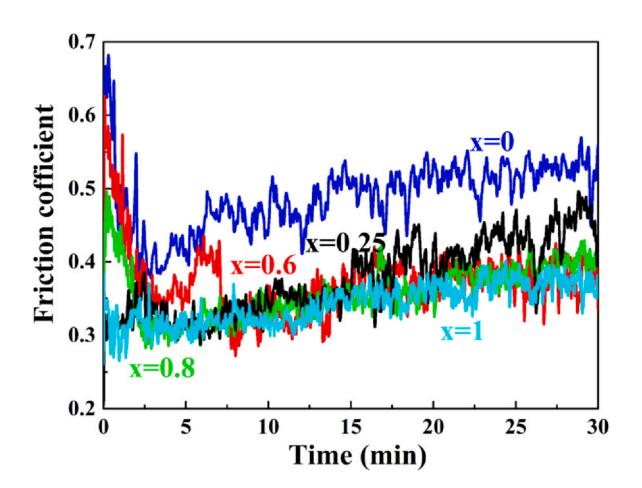


Fig. 6. (a) Lattice constant of FCC structure and (b) the atomic size difference ( $\delta$ ) and the VEC of FeCoNiCrMnMo<sub>x</sub> HEA films as functions of Mo content. With increasing Mo content, the lattice constant and  $\delta$  increase and the VEC decreases, indicating that the addition of the Mo would lead to the severe lattice distortion and the structural instability.



**Fig. 7.** Hardness of FeCoNiCrMnMo<sub>x</sub> (x = 0, 0.25, 0.6, 0.8, 1) HEA films. The hardness of the FeCoNiCrMnMo<sub>x</sub> films gradually increased from ~8.5 GPa (x = 0) to ~12 GPa (x = 1).



**Fig. 8.** Friction coefficient curves of FeCoNiCrMnMo $_x$  (x = 0, 0.25, 0.6, 0.8, 1) HEA films. The friction coefficient decreases from 0.5 to 0.3 (a reduction of 40% at x = 1) with the addition of the Mo element, indicating that the Mo content has a certain effect on the friction coefficient of these films.

The film with high Mo content presents a good friction performance. From the element mapping images, we also see C and O element, possibly coming from C and O absorbed by the sample during storage in the atmosphere. The other elements, i.e., Fe, Co, Ni, Cr, Mn and Mo, are uniformly distributed across the sample surface. In addition, Co, Ni, Mn and Mo elements are less distributed in the wear tracks. Fe and Cr elements are more distributed in the wear tracks, possibly influenced by the 304 stainless steel substrates.

### 4. Discussion

As mentioned above, all the HEA films show columnar structure. It is well known that the mean free path of particle motion is much greater than the distance between the substrates and the targets when the pressure  $\leq 0.1$  Pa during the deposition process [33]. There are few collisions between the particles, and the energy loss is small. Thus, the kinetic energy of the particles is converted into the energy for film growth and crystallization. Therefore, all the films grown present columnar structure. Moreover, the film becomes denser and the grain size decreases with increasing power of the Mo target. High target power exerts strong ion bombardment and sputtering target materials on the films during the deposition process, therefore, more energy is transferred to the films. Consequently, the density of the films increases and the grain size of the films decreases at higher target powers [34]. In addition, during the deposition process, the self-shadowing effect was inhibited owing to the enhancement of the ion bombardment effect. Therefore, as the Mo target power increased, the growth of columnar grain is hindered and the defects decreased.

With the addition of Mo, the phase structure of the film changes from single FCC to the coexistence of FCC and BCC, that can be explained from the perspective of thermodynamics. Guo et al. [31] pointed out that the VEC can be carried out to forecast the phase structures of HEAs. When VEC < 6.87, a single BCC phase exists, FCC and BCC coexistence if  $6.87 \le \text{VEC} < 8.0$ , and a single FCC phase exists if VEC  $\ge 8.0$ . Meanwhile, Zhang et al. [35] pointed out that the  $\delta$  play an important role in phase selection of HEAs and it can be employed to estimate the formation of simple solid solutions. A solid solution phase tends to form when  $\delta \le 6.6\%$ . Previous studies have shown that the addition of alloying elements with a large atomic radius increases the lattice distortion and results in the structure collapse and forming a new phase [36]. For present Mo-doped Cantor alloy films, the FeCoNiCrMn can be regarded as the solvent matrix, and the

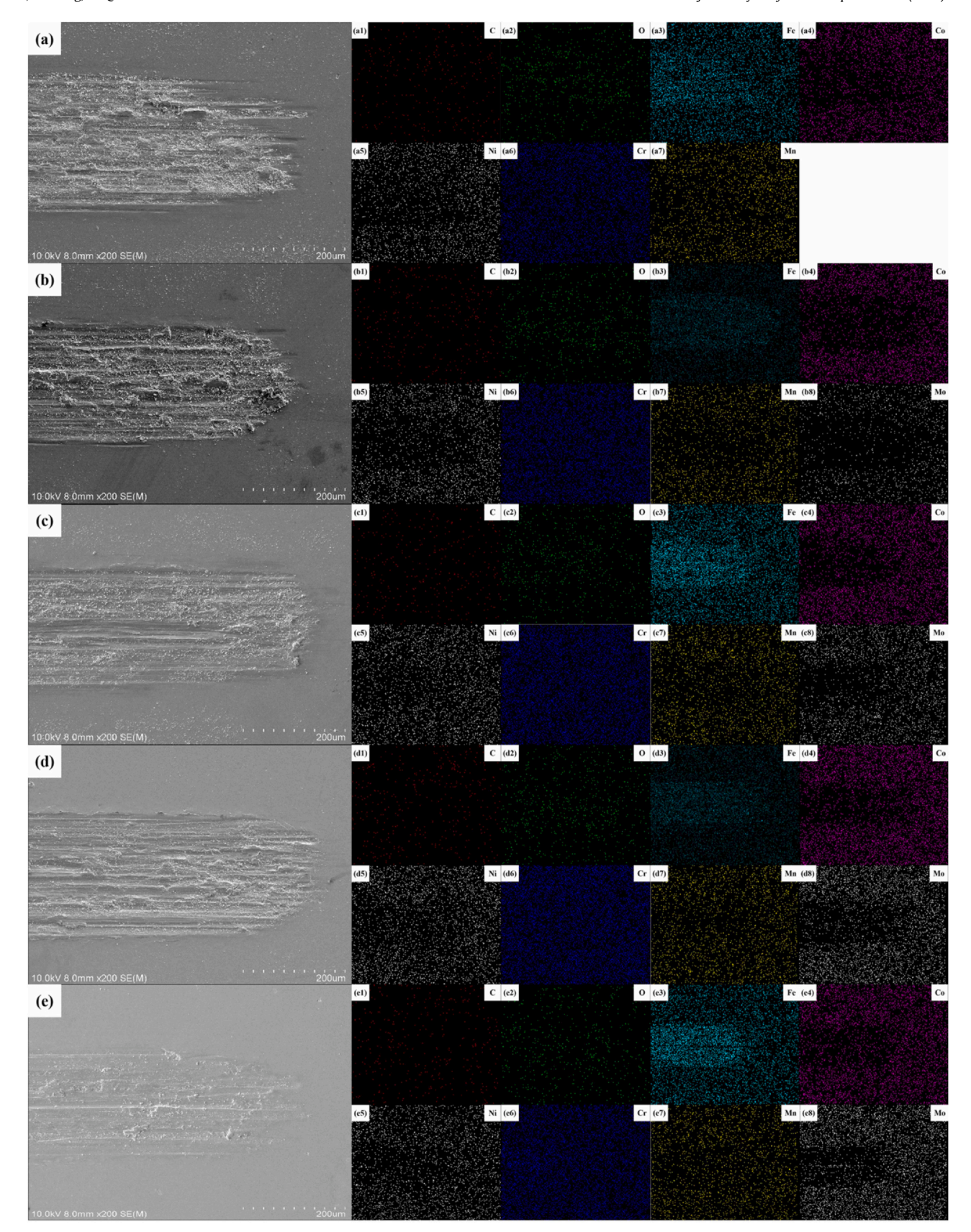


Fig. 9. Friction trajectory surface images of FeCoNiCrMnMo<sub>x</sub> (x = 0, 0.25, 0.6, 0.8, 1) HEA films: (a)x = 0; (b)x = 0.25; (b)x = 0.6; (d)x = 0.8; (e)x = 1, and element mappings of the same region (a1) (a1) (b1) (c1) (d1) (e1): C, (a2) (b2) (c2) (d2) (e2): O, (a3) (b3) (c3) (d3) (e3): Fe, (a4) (b4) (c4) (d4) (e4): Co, (a5) (b5) (c5) (d5) (e5): Ni, (a6) (b6) (c6) (d6) (e6): Cr, (a7) (b7) (c7) (d7) (e7): Mn, (b8) (c8) (d8) (e8): Mo. The width and depth of the wear tracks gradually decline with increasing Mo content, indicating the films with high Mo content present a good friction performance.

larger atomic-sized Mo as the solute. The VEC value of the Mo-doped Cantor alloy film reduces from 8.02 (x = 0) to 7.69 (x = 1), and the phase structure transfers from FCC to the coexistence of FCC and BCC, which is well verified and conforms to Guo's theory [31]. Although the  $\delta$  value of the Mo-doped Cantor alloy films increases from 1.13% (x = 0) to 4.20% (x = 1), it is still less than 6.6%, and thus intermetallic compounds were formed, which confirms Zhang's theory well [35]. In addition, Mo element with BCC phase structure may have a strong influence on the film to form BCC phase. It is worth noting that unlike bulk FeCoNiCrMnMox that has the coexistence of FCC and Sigma phase, the corresponding film does not present the Sigma phase which agreed with the previous study [24]. The rapid cooling rate during the film deposition inhibits the formation of a secondary phase in the films [24].

The hardness of the Mo-doped Cantor alloy films increases obviously with the increase of Mo, attributed to the combined effect of solid solution strengthening, formation of hard BCC phase, grain refinement and the densification of the structure. First, the addition of Mo results in severe local lattice distortion, thus enhancing the solid solution strengthening effect [37]. Compared with Fe, Co, Ni, Cr and Mn atoms with an atomic radius of 1.26, 1.25, 1.24, 1.28 and 1.27 Å, respectively [18], the atomic radius (1.40 Å) of Mo atom is relatively larger. Large atomic radius Mo atoms exist in the crystal structure as the substitutional atoms, forming a substitutional solid solution, which increases the lattice constant and lattice distortion of the film [38]. Thus, the higher the Mo content, the more severe the lattice distortion, the stronger the solid solution strengthening effect, and the higher the hardness. Second, with the addition of Mo, in addition to the FCC phase, harder BCC phase tends to form. It well known that material with FCC structure presents low strength and high plasticity [39]. In contrast, material with BCC structure shows high strength and low plasticity [40]. From the XRD results, the phase structure of the film changes from single FCC to the coexistence of FCC and BCC. Thus, the Mo-doped Cantor alloy film gradually changes from a relatively softer, single FCC phase to a mixture of FCC and harder BCC phases, resulting in the higher hardness at higher Mo contents. Third, grain and phase boundary strengthening also contribute to higher hardness at higher Mo contents [41]. The phase transformation from FCC phase to σ phase caused by the incorporation of Mo into the bulk FeCrNi-CoMn HEA increases the density of phase boundary, which acts as obstacle to dislocation slip and increases the strength [23]. As mentioned above, the averaged grain size of the films decreases with increasing the Mo content. Thus, according to the classical Hall-Petch effect, the films become harder with the reduction of the grain size [42]. Last but not least, previous studies have indicated that densification has an important effect on the hardness of HEA films [43]. As the Mo content increased, the defects and pores of the film decrease, the film becomes denser, thus, the hardness also increases.

As mentioned earlier, COF of the films decreases with the increase of Mo, COF of the Mo-doped Cantor alloy films remain at around 0.3 when x = 1. The largest drop in COF is 40%. There are some debris on the wear tracks of all the films, indicating that the films suffered from abrasive wear. However, with increasing the Mo content of the film, the amount of wear debris, the depth and width of the wear scars all decrease, which indicates that the friction performance of the film has been enhanced with the increase of Mo content. This is owing to the improved hardness of the films at higher Mo contents. According to previous studies, the friction performance of the film is tightly related to the hardness of the film [44]. Therefore, the films with higher hardness tend to show better friction performance. Based on factors aforementioned, Mo doping enhances the mechanical properties of HEA films including hardness and wear resistance.

#### 5. Conclusions

FeCoNiCrMnMo $_{\rm x}$  (x = 0, 0.25, 0.6, 0.8, 1) HEA films prepared by DC magnetron co-sputtering without additional heating show uniform distribution of all the six elements across the film surface. All the films are adhered well to the substrates. With increasing the Mo content, the films become denser, and the phase structure gradually changes from a single FCC phase to a mixture of FCC and BCC phases. Meanwhile, the grain size decreases, lattice constant increases and from no Mo to Mo = 1, the hardness increases by 41% from 8.5 GPa to 12 GPa, the friction coefficient decreases by 40% from 0.5 to 0.3. The addition of Mo greatly improves the mechanical and tribological properties of the FeCoNiCrMn high-entropy film.

### **CRediT** authorship contribution statement

Yiman Zhao: Conceptualization, Methodology, Formal analysis, Writing – original draft, Data curation, Visualization, Validation. Xiaomin Zhang: Methodology, Supervision, Project administration, Funding acquisition. Hui Quan: Conceptualization, Methodology, Data curation. Yujie Chen: Writing – review & editing, Project administration, Funding acquisition. Shu Wang: Methodology, Supervision. Sam Zhang: Writing – review & editing, Conceptualization, Supervision, Project administration, Funding acquisition.

### **Declaration of Competing Interest**

The authors declare that they have no known competing financial interests or personal relationships that could have appeared to influence the work reported in this paper.

### Acknowledgment

This work was financially supported by the Fundamental Research Funds for the Central Universities (SWU118105) and the National Natural Science Foundation of China (51671153). Y.J. Chen acknowledges the support provided by the National Natural Science Foundation of China (52001263).

### References

- F. Cemin, S.R.S. de Mello, C.A. Figueroa, F. Alvarez, Influence of substrate bias and temperature on the crystallization of metallic NbTaTiVZr high-entropy alloy thin films, Surf. Coat. Technol. 421 (2021) 127357, https://doi.org/10.1016/j.surfcoat. 2021127357
- [2] A.D. Pogrebnjak, V.M. Beresnev, K.V. Smyrnova, Ya.O. Kravchenko, P.V. Zukowski, G.G. Bondarenko, The influence of nitrogen pressure on the fabrication of the two-phase superhard nanocomposite (TiZrNbAlYCr)N coatings, Mater. Lett. 211 (2018) 316–318. https://doi.org/10.1016/j.matlet.2017.09.121
- [3] Y. Yang, Q.F. He, Lattice distortion in high-entropy alloys, Acta Metall. Sin. 57 (2021) 385–392, https://doi.org/10.11900/0412.1961.2020.00359
- [4] A.D. Pogrebnjak, A.A. Bagdasaryan, I.V. Yakushchenko, V.M. Beresnev, The structure and properties of high-entropy alloys and nitride coatings based on them, Russ. Chem. Rev. 83 (2014) 1027–1061, https://doi.org/10.1070/ RC2014v083n11ABFH004407
- [5] M.H. Tsai, J.W. Yeh, High-entropy alloys: a critical review, Mater. Res. Lett. 2.3 (2014) 107–123, https://doi.org/10.1080/21663831.2014.912690
- [6] N.S. Peighambardoust, A.A. Alamdari, U. Unal, A. Motallebzadeh, In vitro bio-compatibility evaluation of Ti<sub>1.5</sub>ZrTa<sub>0.5</sub>Nb<sub>0.5</sub>Hf<sub>0.5</sub> refractory high-entropy alloy film for orthopedic implants: microstructural, mechanical properties and corrosion behavior, J. Alloy. Compd. 883 (2021) 160786, https://doi.org/10.1016/j.jallcom.2021.160786
- [7] Y.L. Liu, F. Zhang, Z.Y. Huang, Q. Zhou, Y. Ren, Y. Du, H.F. Wang, Mechanical and dry sliding tribological properties of CoCrNiNb<sub>x</sub> medium-entropy alloys at room temperature, Tribol. Int. 163 (2021) 107160, https://doi.org/10.1016/j.triboint. 2021.107160
- [8] S.F. Sun, H. Liu, J.B. Hao, H.F. Yang, Microstructural evolution and corrosion behavior of CoCrFeNiAl<sub>x</sub>Mn<sub>(1-x)</sub> dual-phase high-entropy alloy coatings prepared by laser cladding, J. Alloy. Compd. 886 (2021) 161251, https://doi.org/10.1016/j.jallcom.2021.161251
- [9] L.X. Yang, H.L. Ge, J. Zhang, T. Xiong, Q.Q. Jin, Y.T. Zhou, X.H. Shao, B. Zhang, Z.W. Zhu, S.J. Zheng, X.L. Ma, High He-ion irradiation resistance of CrMnFeCoNi

- high-entropy alloy revealed by comparison study with Ni and 304SS, J. Mater. Sci. Technol. 35 (2019) 300–305, https://doi.org/10.1016/j.jmst.2018.09.050
- [10] A.D. Pogrebnjak, I.V. Yakushchenko, O.V. Bondar, V.M. Beresnev, K. Oyoshi, O.M. Ivasishin, H. Amekura, Y. Takeda, M. Opielak, C. Kozak, Irradiation resistance, microstructure and mechanical properties of nanostructured (TiZrHfVNbTa)N coatings, J. Alloy. Compd. 679 (2016) 155–163, https://doi.org/10.1016/j.jallcom.2016.04.064
- [11] H. Zhang, Y.Z. He, Y. Pan, Enhanced hardness and fracture toughness of the laser-solidified FeCoNiCrCuTiMoAlSiB<sub>0.5</sub> high-entropy alloy by martensite strengthening, Scr. Mater. 69 (2013) 342–345, https://doi.org/10.1016/j.scriptamat.2013. 05.020
- [12] F.X. Ye, Z.P. Jiao, S. Yan, L. Guo, L.Z. Feng, J.X. Yu, Microbeam plasma arc remanufacturing: effects of Al on microstructure, wear resistance, corrosion resistance and high temperature oxidation resistance of Al<sub>x</sub>CoCrFeMnNi highentropy alloy cladding layer, Vacuum 174 (2020) 109178, https://doi.org/10.1016/j.vacuum.2020.109178
- [13] H. Wang, D.K. Chen, X.H. An, Y. Zhang, S.J. Sun, Y.Z. Tian, Z.F. Zhang, A.G. Wang, J.Q. Liu, M. Song, S.P. Ringer, T. Zhu, X.Z. Liao, Deformation-induced crystalline-to-amorphous phase transformation in a CrMnFeCoNi high-entropy alloy, Sci. Adv. 7 (2021) eabe3105, https://doi.org/10.1126/sciadv.abe3105
- [14] X. Sun, H.L. Zhang, W. Li, X.D. Ding, Y.Z. Wang, L. Vitos, Generalized stacking fault energy of Al-doped CrMnFeCoNi high-entropy alloy, Nanomaterials 10 (2020) 59, https://doi.org/10.3390/nano10010059
- [15] J.K. Xiao, H. Tan, Y.Q. Wu, J. Chen, C. Zhang, Microstructure and wear behavior of FeCoNiCrMn high entropy alloy coating deposited by plasma spraying, Surf. Coat. Technol. 385 (2020) 125430, https://doi.org/10.1016/j.surfcoat.2020.125430
- [16] Z. Wang, C. Wang, Y.L. Zhao, T.H. Huang, C.L. Li, J.J. Kai, C.T. Liu, C.H. Hsueh, Growth, microstructure and mechanical properties of CoCrFeMnNi high entropy alloy films, Vacuum 179 (2020) 109553, https://doi.org/10.1016/j.vacuum.2020. 109553
- [17] H. Jiang, H.Z. Zhang, T.D. Huang, Y.P. Lu, T.M. Wang, T.J. Li, Microstructures and mechanical properties of Co<sub>2</sub>Mo<sub>x</sub>Ni<sub>2</sub>VW<sub>x</sub> eutectic high entropy alloys, Mater. Des. 109 (2016) 539–546, https://doi.org/10.1016/j.matdes.2016.07.113
- [18] Y.C. Hsu, C.L. Li, C.H. Hsueh, Effects of Al addition on microstructures and mechanical properties of CoCrFeMnNiAl<sub>x</sub> high entropy alloy films, Entropy 22 (2020) 2, https://doi.org/10.3390/e22010002
- [19] L.Z. Medina, M.V. Tavares da Costa, E.M. Paschalidou, G. Lindwall, L. Riekehr, M. Korvela, S. Fritze, S. Kolozsvári, E.K. Gamstedt, L. Nyholm, U. Jansson, Enhancing corrosion resistance, hardness, and crack resistance in magnetron sputtered high entropy CoCrFeMnNi coatings by adding carbon, Mater. Des. 205 (2021) 109711. https://doi.org/10.1016/j.matdes.2021.109711
- (2021) 109711, https://doi.org/10.1016/j.matdes.2021.109711
  [20] B.B. Xin, A.J. Zhang, J.S. Han, J.H. Meng, Improving mechanical properties and tribological performance of Al<sub>0.2</sub>Co<sub>1.5</sub>CrFeNi<sub>1.5</sub>Ti<sub>0.5</sub> high entropy alloys via doping Si, J. Alloy. Compd. 869 (2021) 159122, https://doi.org/10.1016/j.jallcom.2021.
- [21] W. Wu, L. Jiang, H. Jiang, X.M. Pan, Z.Q. Cao, D.W. Deng, T.M. Wang, T.J. Li, Phase evolution and properties of Al<sub>2</sub>CrFeNiMo<sub>x</sub> high-entropy alloys coatings by laser cladding, J. Therm. Spray. Technol. 24 (2015) 1333–1340, https://doi.org/10.1007/s11666-015-0303-6
- [22] Z.Z. Niu, Y.Z. Wang, C. Geng, J. Xu, Y. Wang, Microstructural evolution, mechanical and corrosion behaviors of as-annealed CoCrFeNiMo<sub>x</sub> (x = 0, 0.2, 0.5, 0.8, 1) high entropy alloys, J. Alloy. Compd. 820 (2020) 153273, https://doi.org/10.1016/j.iall.com.2019.153273
- [23] G. Qin, R.R. Chen, H.T. Zheng, H.Z. Fang, L. Wang, Y.Q. Su, J.J. Guo, H.Z. Fu, Strengthening FCC-CoCrFeMnNi high entropy alloys by Mo addition, J. Mater. Sci. Technol. 35 (2019) 578–583, https://doi.org/10.1016/j.jmst.2018.10.009
- [24] T.H. Huang, C.H. Hsueh, Microstructures and mechanical properties of (CoCrFeMnNi)<sub>100-x</sub>Mo<sub>x</sub> high entropy alloy films, Intermetallics 135 (2021) 107236, https://doi.org/10.1016/j.intermet.2021.107236
- [25] X.W. Shi, X.H. Yu, C.W. Nie, F.J. Li, S. Zhang, Controlled growth of nanocrystalline aluminum nitride films for full color range, Ceram. Int. 47 (2021) 21546–21553, https://doi.org/10.1016/j.ceramint.2021.04.166

- [26] N. Laegreid, G.K. Wehner, Sputtering yields of metals for Ar<sup>+</sup> and Ne<sup>+</sup> ions with energies from 50 to 600 eV, J. Appl. Phys. 32 (1961) 365–369, https://doi.org/10.
- [27] J.J. Wang, S.Y. Chang, F.Y. Ouyang, Effect of substrate bias on the microstructure and properties of (AlCrSiNbZr)N<sub>x</sub> high entropy nitride thin film, Surf. Coat. Technol. 393 (2020) 125796. https://doi.org/10.1016/j.surf.coat.2020.125796
- [28] A.L. Patterson, The scherrer formula for X-ray particle size determination, Phys. Rev. 56 (1939) 978–982, https://doi.org/10.1103/PhysRev.56.978
- [29] W.Y. Yu, W. Li, P. Liu, K. Zhang, F.C. Ma, X.H. Chen, R. Feng, P.K. Liaw, Silicon-content-dependent microstructures and mechanical behavior of (AlCrTiZrMo)-Si<sub>x</sub>-N high-entropy alloy nitride film, Mater. Des. 203 (2021) 109553, https://doi.org/10.1016/j.matdes.2021.109553
- [30] T.X. Li, Y.P. Lu, Z.Q. Cao, T.M. Wang, T.J. Li, Opportunity and challenge of refractory high-entropy alloys in the field of reactor structural materials, Acta Metall. Sin. 57 (2021) 42–54, https://doi.org/10.1016/10.11900/0412.1961.2020.00293
- [31] S. Guo, C. Ng, J. Lu, C.T. Liu, Effect of valence electron concentration on stability of fcc or bcc phase in high entropy alloys, J. Appl. Phys. 109 (2011) 103505, https:// doi.org/10.1063/1.3587228
- [32] B. Schuh, F. Mendez-Martin, B. Völker, E.P. George, H. Clemens, R. Pippan, A. Hohenwarter, Mechanical properties, microstructure and thermal stability of a nanocrystalline CoCrFeMnNi high-entropy alloy after severe plastic deformation, Acta Mater. 96 (2015) 258–268, https://doi.org/10.1016/j.actamat.2015.06.025
- [33] S. Mahieu, P. Ghekiere, D. Depla, R. De Gryse, Biaxial alignment in sputter deposited thin films, Thin Solid Films 515 (2006) 1229–1249, https://doi.org/10.1016/j.psf.2006.06.027
- [34] S.Y. Lin, S.Y. Chang, C.J. Chang, Y.C. Huang, Nanomechanical properties and deformation behaviors of multi-component (AlCrTaTiZr)N<sub>x</sub>Si<sub>y</sub> high-entropy coatings, Entropy 16 (2014) 405–417, https://doi.org/10.3390/e16010405
- [35] X. Yang, S.Y. Chen, J.D. Cotton, Y. Zhang, Phase stability of low-density, multi-principal component alloys containing aluminum, magnesium, and lithium, JOM J. Miner. Met. Mater. Soc. 66 (2014) 2009–2020, https://doi.org/10.1007/s11837-014-1059-z
- [36] X.B. Feng, W. Fu, J.Y. Zhang, J.T. Zhao, J. Li, K. Wu, G. Liu, J. Sun, Effects of nanotwins on the mechanical properties of Al<sub>x</sub>CoCrFeNi high entropy alloy thin films, Scr. Mater. 139 (2017) 71–76, https://doi.org/10.1016/j.scriptamat.2017.06.
- [37] C.R. LaRosa, M. Shih, C. Varvenne, M. Ghazisaeidi, Solid solution strengthening theories of high-entropy alloys, Mater. Charact. 151 (2019) 310–317, https://doi. org/10.1016/j.matchar.2019.02.034
- [38] X.F. Yao, J.P. Wei, Y.K. Lv, T.Y. Li, Precipitation σ phase evoluation and mechanical properties of (CoCrFeMnNi)<sub>97.02</sub>Mo<sub>2.98</sub> high entropy alloy, Acta Metall. Sin. 56 (2020) 769–775, https://doi.org/10.1016/10.11900/0412.1961.2019.00330
- [39] A.D. Pogrebnjak, A.A. Bagdasaryan, I.V. Yakushchenko, V.M. Beresnev, The structure and properties of high-entropy alloys and nitride coatings based on them, Russ. Chem. Rev. 83 (2014) 1027–1061, https://doi.org/10.1070/RCR4407
- [40] W.J. Kim, H.T. Jeong, H.K. Park, K. Park, T.W. Na, E. Choi, The effect of Al to high-temperature deformation mechanisms and processing maps of Al<sub>0.5</sub>CoCrFeMnNi high entropy alloy, J. Alloy. Compd. 802 (2019) 152–165, https://doi.org/10.1016/i.iallcom.2019.06.099
- [41] J. Skamat, O. Cernasejus, A.V. Valiulis, R. Lukauskait, N. Visniakov, Improving hardness of Ni-Cr-Si-B-Fe-C thermal sprayed coatings through grain refinement by vibratory treatment during refusion, Mater. Sci. 21 (2015) 207–214, https:// doi.org/10.5755/j01.mm.21.2.6833
- [42] S. Zhang, Thin Films and Coatings: Toughening and Toughness Characterization, Crc Press, 2015.
- [43] W. Li, P. Liu, Peter K. Liaw, Microstructures and properties of high-entropy alloy films and coatings: a review, Mater. Res. Lett. 6 (2018) 199–229, https://doi.org/ 10.1080/21663831.2018.1434248
- [44] C.H. Liang, W.L. Wang, C.F. Huang, H.Y. Tsai, C.C. Yang, The influence of microstructural variations on mechanical and tribological properties of low-friction TiC/diamond-like carbon nanocomposite films, Ceram. Int. 40 (2014) 13329–13337, https://doi.org/10.1016/j.ceramint.2014.05.047